Research Article

Nano Research
2022, 15(6): 4950–4957

ISSN 1998-0124 CN 11-5974/O4
https://doi.org/10.1007/s12274-022-4112-1

Ultrastable bimetallic Fe_2Mo for efficient oxygen reduction reaction in pH-universal applications

Jue Hu[1,§] (✉), Chengxu Zhang[1,§], Mingzi Sun[2], Qianglong Qi[1], Shanxiong Luo[1], Hongchuan Song[3], Jingyi Xiao[4], Bolong Huang[2] (✉), Michael K. H. Leung[4] (✉), and Yingjie Zhang[1] (✉)

[1] *The Engineering Laboratory of Advanced Battery and Materials of Yunnan Province, Kunming University of Science and Technology, Kunming 650093, China*
[2] *Department of Applied Biology and Chemical Technology, The Hong Kong Polytechnic University, Hung Hom, Kowloon, Hong Kong, China*
[3] *School of Energy and Environment Science, Yunnan Normal University, Kunming 650500, China*
[4] *Ability R&D Energy Research Centre, School of Energy and Environment, City University of Hong Kong, Hong Kong, China*
[§] *Jue Hu and Chengxu Zhang contributed equally to this work.*

Received: 27 November 2021 / **Revised:** 22 December 2021 / **Accepted:** 22 December 2021

ABSTRACT

Iron-based nanostructures represent an emerging class of catalysts with high electroactivity for oxygen reduction reaction (ORR) in energy storage and conversion technologies. However, current practical applications have been limited by insufficient durability in both alkaline and acidic environments. In particular, limited attention has been paid to stabilizing iron-based catalysts by introducing additional metal by the alloying effect. Herein, we report bimetallic Fe_2Mo nanoparticles on N-doped carbon (Fe_2Mo/NC) as an efficient and ultra-stable ORR electrocatalyst for the first time. The Fe_2Mo/NC catalyst shows high selectivity for a four-electron pathway of ORR and remarkable electrocatalytic activity with high kinetics current density and half-wave potential as well as low Tafel slope in both acidic and alkaline medias. It demonstrates excellent long-term durability with no activity loss even after 10,000 potential cycles. Density functional theory (DFT) calculations have confirmed the modulated electronic structure of formed Fe_2Mo, which supports the electron-rich structure for the ORR process. Meanwhile, the mutual protection between Fe and Mo sites guarantees efficient electron transfer and long-term stability, especially under the alkaline environment. This work has supplied an effective strategy to solve the dilemma between high electroactivity and long-term durability for the Fe-based electrocatalysts, which opens a new direction of developing novel electrocatalyst systems for future research.

KEYWORDS

oxygen reduction reaction, Fe_2Mo bimetallic nanoparticles, zeolitic imidazolate frameworks (ZIFs), ultralong stability, superior oxygen reduction reaction (ORR) performance

1 Introduction

The increasingly serious crises about global warming, environmental pollution, and energy security have raised the demand for environmental-friendly renewable energy sources instead of fossil fuels. Efficient fuel cells and metal–air batteries are arguably the most promising sustainable energy conversion technologies that are limited by the sluggish kinetics of the cathodic electrochemical oxygen reduction reaction (ORR), and as a result, hindered their implementation [1–3]. Although platinum group metal (PGM) catalysts have served as the most efficient and preferred choices for ORR, their high cost and scarcity, as well as poor durability, have motivated the exploration of competitive alternatives of PGM-free materials as highly efficient and durable ORR catalysts [4–7]. Numerous efforts have been devoted to finding alternative catalysts including non-metallic carbon nanostructures [8], non-precious metals [9, 10], metal macrocycles [11, 12], transition metal oxides [13], carbides [14–16], sulfides [17], nitrides [18], and single atomic metal catalysts [19, 20]. Among them, iron-based material, because of the high earth abundance and promising catalytic activities, is considered as one of the most potential alternatives of PGM catalysts [21–23]. For current developments of novel non-PGM electrocatalysts, the determination of the ORR active sites is one of the most critical challenges, especially for those electrocatalysts imparted during the pyrolysis step. However, Fe-based catalysts still suffer from limited ORR performance as the Fe atoms rapidly leached both in acidic and alkaline medias [24, 25]. Single atomic catalysts owning isolated active sites can greatly increase the atomic utilization [26, 27]. Intensive studies focused on the single atomic iron, especially $Fe\text{-}N_4$, which acted as the active site for efficient ORR electrocatalysis in alkaline media, demonstrating a synergistic effect between the C–N bonding environment in nitrogen doped porous carbon supports and the edge-hosted Fe sites [19, 23, 28]. Interestingly, Wu et al. discovered that Fe-N-C sites also had a Pt like ORR catalytic performance in acidic media [21, 29–31]. Recently, Li et al. have reported adjunct dual

Address correspondence to Jue Hu, hujue@kust.edu.cn; Bolong Huang, bhuang@polyu.edu.hk; Michael K. H. Leung, mkh.leung@cityu.edu.hk; Yingjie Zhang, zyjkmust@126.com

atomic sites based on Fe-N_4/Pt-N_4@NC, where Pt sites can effectively optimize ORR performances through the rehybridization of Fe-3d and O-2p orbitals, leading to remarkable performances and durability in Zn–air battery [32]. Nevertheless, it remains a key challenge to synthesize highly active and durable iron-based catalysts for ORR [20].

Bao and coworkers encapsulated Fe nanoparticles into carbon nanotubes (CNTs) and found that electrons could transfer from Fe particles to CNTs, leading to a decreased local work function on the carbon surface, and as a result, an arising ORR catalytic performance of the pod-like CNT covered Fe nanoparticles [10]. Recent studies show extensive evidence that encapsulation of catalyst nanoparticles into nitrogen doped carbon nanoshells leads to an enhancement in the catalytic activity due to the improved adsorption of O_2 and decomposition of peroxide intermediates and stability attributed to the carbon shell protection compared to the corresponding non-protected catalysts [33–35]. Furthermore, bimetallic particle catalysts such as Mn-Co, Fe-Co, Fe-Pt, and Ni-Pt, have been demonstrated to outperform their pure monometallic component catalysts [9, 36–38]. Huang and coworkers doped Pt_3Ni octahedra supported on carbon with transition metals such as Mo, V, Mg, Fe, Co, W, and Ru, and revealed that the doping of Mo could shift the oxygen binding energies at the thermodynamically favored sites closer to the peak of the volcano plot. As a result of these shifts, some sites became highly active for ORR catalysis [6]. Doping Mo also can stabilize both Ni and Pt atoms against dissolution through the formation of relatively strong Mo–Pt and Mo–Ni bonds [6].

Herein, we report bimetallic Fe_2Mo nanoparticles on N-doped carbon (Fe_2Mo/NC) as an efficient and ultra-stable ORR electrocatalyst for the first time. The robust carbon encapsulated Fe_2Mo bimetallic catalyst with efficient ORR catalytic activity and durability in both alkaline and acidic environments derived from zeolitic imidazolate frameworks (ZIFs). ZIFs, as a subclass of metal–organic frameworks, are excellent precursors for nanocarbon structures owing to their abundant carbon and nitrogen species. Highly graphitized carbon frameworks or quasi-amorphous carbon with graphitic edge planes can be prepared through the pyrolysis of ZIFs [36]. Usually, the metal nanoparticles covered by carbon shells and exposed outside the carbon frameworks coexist after the carbonization process. Strong acid leaching can remove the exposed metal particles and leave the carbon encapsulated metal nanoparticles, which are recognized as active components for ORR electrocatalysis [34]. The resulting carbon encapsulated Fe_2Mo bimetallic catalyst exhibits significant enhancement in the ORR catalytic activity and durability when compared to the monometallic Fe/NC and the commercial Pt/C catalysts. ORR catalytic activities in terms of half-wave potentials (0.91 V in 0.1 M KOH solution and 0.8 V in 0.5 M H_2SO_4 solution) and kinetic current densities (82.28 mA/cm^2 at 0.85 V in 0.1 M KOH solution and 37.62 mA/cm^2 at 0.75 V in 0.5 M H_2SO_4 solution) compare favorably with most highly active PGM-free ORR catalysts reported so far. Density functional theory (DFT) calculations have investigated the electroactivity of the formed Fe_2Mo, which displays the optimized electronic structure for fast electron transfer from electrocatalysts to intermediates. Moreover, the Fe-3d and Mo-4d orbitals form the electronic shell to protect the electrocatalyst to achieve superior stability.

2 Results and discussion

Fe-doped ZIF-8 (Fe-ZIF-8) and Mo,Fe-codoped ZIF-8 (FeMo-ZIF-8) precursors were synthesized under the same condition and followed the same procedure of the synthesis of ZIF-8. Powder X-ray diffraction (XRD) patterns of the Fe-ZIF-8 and FeMo-ZIF-8 well match ZIF-8 with the diffraction peaks at 2θ = 7.2°, 10.1°, 12.5°, and 17.9° assigned to the (011), (002), (112), and (222) planes of ZIF-8 (Fig. S1(a) in Electronic Supplementary Material (ESM)), respectively [39], indicating that the adding of Fe and Mo is not expected to result in a change in the crystal structure. The pyrolysis at 1,000 °C converts the ZIF-8, Fe-ZIF-8, and FeMo-ZIF-8 precursors into nitrogen decorated carbon (NC) based materials which were labeled as NC, Fe-NC, and FeMo-NC, respectively. The Fe/NC and Fe_2Mo/NC catalysts were synthesized by subsequent acid leaching of Fe-NC and FeMo-NC, respectively. Experimental details were provided in the ESM. As shown in Fig. S1(b), the XRD pattern of acid leached NC sample presents three diffraction peaks at 2θ = 25°, 31°, and 44°, which are corresponding to the graphitized carbon (JCPDS card no. 46-0944). The diffraction peaks at 49.5° and 56.6° of the Fe/NC sample are associated with the (102) and (103) planes of metallic iron (JCPDS card no. 50-1275), respectively, suggesting the existence of metallic Fe in the Fe/NC catalyst. The diffraction peaks at 38.1°, 41.4°, and 45.9° of the standard Fe_2Mo/NC sample (JCPDS card no. 06-0622) are not detected in the XRD pattern of NC and Fe/NC, which are corresponding to the (110), (103), and (201) planes of Fe_2Mo, respectively, indicating the generation of bimetallic Fe_2Mo alloy in the Fe_2Mo/NC catalyst.

The morphologies of the Fe/NC and Fe_2Mo/NC catalysts were characterized by scanning electron microscopy (SEM) and transmission electron microscopy (TEM). SEM images present a uniform dodecahedron shaped morphology with a size of about 50 nm for Fe/NC and Fe_2Mo/NC catalysts, which is similar to that of NC (Figs. 1(a) and 1(b), and Fig. S2 in the ESM). In Figs.S3 and S4 in the ESM, it is evident that there is no obvious difference of morphology for the Fe/NC and Fe_2Mo/NC catalysts from Fe-ZIF-8 and FeMo-ZIF-8 precursors, indicating that the catalysts could retain their initial dodecahedral shape after the pyrolysis and acid leaching processes. SEM-energy dispersive X-ray spectroscopy (SEM-EDS) elemental spectra confirm the existence of Fe and Mo in the Fe_2Mo/NC catalyst. The Fe, Mo, and Zn loadings in Fe/NC and Fe_2Mo/NC catalysts are quantified by the inductively coupled plasma optical emission spectroscopy (ICP-OES) analysis, which are in good agreement with the SEM-EDS spectra (Table S1 in the ESM). The ultra-low content of Zn in both Fe/NC (0.024 wt.%) and Fe_2Mo/NC (0.023 wt.%) catalysts proves the complete removal of Zn after the pyrolysis and acid leaching steps. We also notice that the molar ratio of Fe and Mo obtained from ICP-OES is 2.1 for the Fe_2Mo/NC catalyst, which is closed to the stoichiometric coefficient 2 for that of Fe_2Mo molecule. Metallic nanoparticles are observed by scanning transmission electron microscope (STEM) images of Fe/NC and Fe_2Mo/NC (Figs. S5(a) and S6(a) in the ESM), which are identified by bright dots marked with red cycles. The TEM images show carbon encapsulated nanoparticles with a diameter about 14 nm of Fe/NC and 8 nm of Fe_2Mo/NC (Figs. S5–S7 in the ESM). As shown in the high-resolution transmission electron microscopy (HRTEM) image (Fig. 1(c)), the *d*-spacing of 0.18 nm corresponds to the (102) facet of metallic iron, confirming the existence of Fe nanoparticles in the Fe/NC catalyst. The highly ordered lattice planes in the HRTEM images of Fe_2Mo/NC catalyst are clearly visible in Fig. 1(d) and Fig. S6 in the ESM. The lattice fringes with a distance of 0.22 nm correspond to the (103) facet of Fe_2Mo, confirming the existence of Fe_2Mo nanoparticles in the Fe_2Mo/NC catalyst, which is in good consistent with the analyses of XRD and ICP. Element mapping and corresponding EDS images shown in Fig. 1(e) present the uniform distribution of C, N, Fe, and Mo in the Fe_2Mo/NC catalyst at the given resolution.

X-ray photoelectron spectroscopy (XPS) was proved effective to determine the chemical bonding nature of the C, N, and Fe

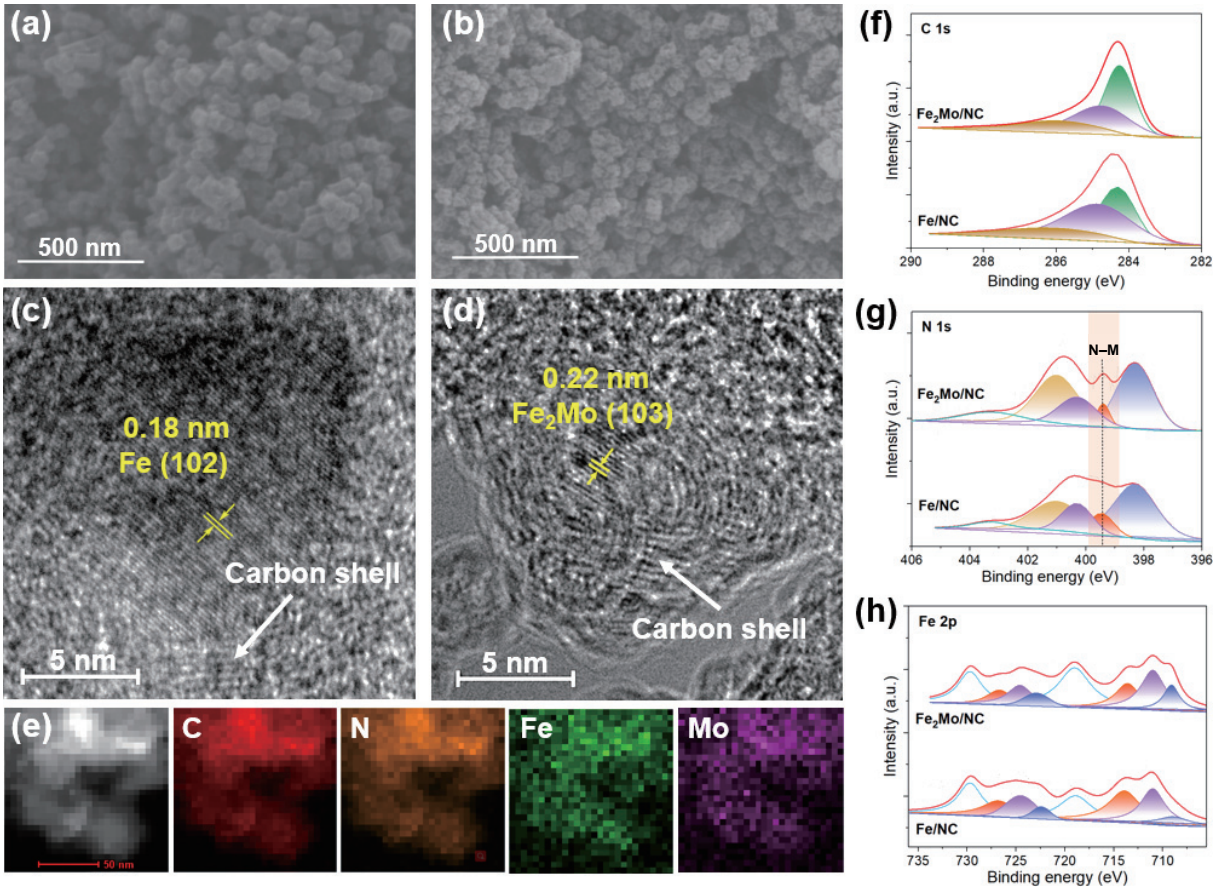

Figure 1 Morphology and structure characterization of the Fe_2Mo/NC catalyst. Field emission scanning electron microscopy (FESEM) images of (a) Fe/NC and (b) Fe_2Mo/NC. HR-TEM images of (c) Fe/NC and (d) Fe_2Mo/NC. (e) STEM image and corresponding elemental maps of C, N, Fe, and Mo of the Fe_2Mo/NC catalyst. High-resolution (f) C 1s, (g) N 1s, and (h) Fe 2p XPS data of the Fe/NC and Fe_2Mo/NC catalysts.

species in the catalysts. Figures 1(f)–1(h) present the changes in the XPS patterns between the Fe/NC and Fe_2Mo/NC catalysts. High-resolution C 1s spectra can be fitted into three characteristic peaks at the binding energy of 284.4, 284.8, and 286.0 eV, corresponding to C–C, C=C, and C–N/O, respectively (Fig. 1(f)) [40]. The N 1s spectra reveal the coexistence of five types of nitrogen species, pyridinic N (398.3 eV), metal-N_x (399.4 eV), pyrrolic N (400.3 eV), graphitic N (401.1 eV), and oxidized N (403.3 eV), indicating the existence of metal-N_x species in both Fe/NC and Fe_2Mo/NC catalysts (Fig. 1(g)) [41]. The quantitative analysis of the N 1s spectra reveals a higher percentage of the metal-N_x species in Fe/NC (0.60 at.%) than that in Fe_2Mo/NC (0.29 at.%). Figure S8 in the ESM shows the Mo 3d spectra of Fe/NC and Fe_2Mo/NC. The doublet at 227.8 and 231.8 eV is assigned as the zero-valence Mo ($3d_{3/5}$ and $3d_{2/5}$, respectively), and the other doublet at 228.9 and 234.6 eV is attributed to the Mo^{4+} for the Fe_2Mo/NC catalyst, further indicating the existence of metallic molybdenum in the Fe_2Mo/NC catalyst [42]. The high-resolution Fe 2p spectra of Fe/NC and Fe_2Mo/NC show three doublets ($2p_{3/2}$ and $2p_{1/2}$). The doublet at 713.8 and 726.7 eV corresponds to Fe^{3+}, and the doublet at 711.0 and 724.5 eV are assigned as Fe^{2+}, further supporting the existence of Fe-N_x species in both Fe/NC and Fe_2Mo/NC (Fig. 1(h)) [43]. The doublet at 708.9 and 722.4 eV corresponds to zero-valence Fe, further supporting the existence of metallic iron in both Fe/NC and Fe_2Mo/NC catalysts, which is consistent with the results of TEM and XRD [44].

Cyclic voltammetry (CV) curves (Fig. S9 in the ESM) are found to exhibit oxygen reduction peaks for both the Fe/NC and Fe_2Mo/NC catalysts in O_2-saturated 0.1 M KOH solution, but not in the N_2-saturated KOH solution. A slightly positive shift of the potential of the oxide reduction peak is observed for the Fe_2Mo/NC catalyst when compared with Fe/NC catalyst, indicating a decrease of desorption free energy of oxide species from the Fe_2Mo bimetallic surface. The dependence of the ORR activity among different catalysts can be explained by using the electrochemically accessible surface area reflected from the double-layer capacitance (C_{dl}) of the non-noble metal catalysts [29]. As shown in Fig. S10 in the ESM that C_{dl} values for Fe/NC and Fe_2Mo/NC catalysts are almost the same, indicating a similar electrochemically accessible surface area for the Fe/NC and Fe_2Mo/NC catalysts. The ORR polarization curves for Fe_2Mo/NC, Fe/NC, and commercial Pt/C catalysts on a rotating disk electrode (RDE) in O_2-saturated 0.1 M KOH solution at 1,600 rpm are shown in Fig. 2(a). The half wave potential ($E_{1/2}$) in the ORR polarization curve for Fe_2Mo/NC catalyst is 0.91 V, which is 72 and 32 mV higher than those of commercial Pt/C and Fe/NC catalysts, respectively, indicating a much higher ORR electrocatalytic activity for the Fe_2Mo/NC catalyst. The value of diffusion current density indicates a complete reduction of O_2 to H_2O (four-electron process) on the surface of the Fe_2Mo/NC catalyst. To assess the ORR pathway of Fe_2Mo/NC, the RDE measurements at various rotation rates were carried out (Fig. S11 in the ESM). According to the Koutecky–Levich plot which shows linear relationships between j_k^{-1} and $\omega^{-1/2}$ (where ω is the electrode rotating rate), the electron-transfer number (n) is calculated to be ~ 4 over the potential range from 0.3 to 0.7 V, approaching the theoretical value of a four-electron ORR pathway for the Fe_2Mo/NC catalyst. The ORR selectivity (HO_2^- yield in alkaline media) of all catalysts is further evaluated using a rotating ring-disk electrode (RRDE) in O_2-saturated 0.1 M KOH electrolyte. RRDE measurements demonstrate that the Fe/NC and Fe_2Mo/NC

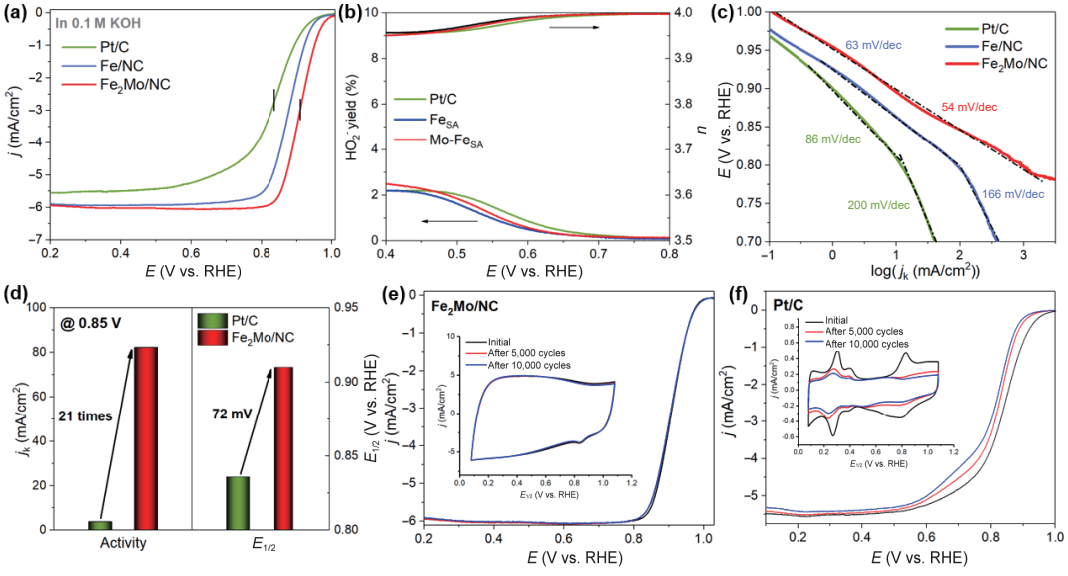

Figure 2 Performance of catalysts for the oxygen reduction in alkaline media. (a) Linear voltammetry curves of commercial Pt/C, Fe/NC, and Fe_2Mo/NC catalysts recorded in O_2-saturated 0.1 M KOH at 1,600 rpm. (b) Electron transfer number and peroxide yield calculated from the RRDE measurements for Pt/C, Fe/NC, and Fe_2Mo/NC catalysts. (c) Mass transport corrected Tafel plots of commercial Pt/C, Fe/NC, and Fe_2Mo/NC catalysts. (d) Comparison of the kinetic current density at 0.85 V and half-wave potential for the commercial Pt/C and Fe_2Mo/NC catalysts. ORR polarization curves and (inset) corresponding CV curves of (e) the Fe_2Mo/NC and (f) commercial Pt/C catalysts before and after 5,000 and 10,000 cycles between 0.6 and 1.0 V.

catalysts exhibit a low HO_2^- yield of about 2.5% with a high electron-transfer number of about 3.95, suggesting a high-efficiency four-electron ORR pathway (Fig. 2(b)). To get a deeper insight into the enhancement of the ORR activity on the distinct Fe_2Mo bimetallic surface, mass transport corrected Tafel plots based on kinetic current density (j_k) for Fe_2Mo/NC, Fe/NC, and commercial Pt/C catalysts are analyzed. As shown in Fig. 2(c), the Tafel plots on the surfaces of Fe/NC and Pt/C catalysts in 0.1 M KOH solution are well fitted with two Tafel slopes: a lower Tafel slope at the high potential region and a higher Tafel slope at the low potential region due to the sluggish ORR kinetics by the site blocking and electronic effects of adsorbed OH_{ad} on the active sites [7]. It can be clearly observed from Fig. 2(c) that a low Tafel slope of 54 mV/dec is fitted for the Fe_2Mo/NC catalyst at both the high and low potential regions, indicating easier desorption of OH_{ad} from the Fe_2Mo bimetallic surface and as a result a favorable ORR kinetics of the Fe_2Mo/NC catalyst (further demonstrated by DFT calculation discussed below). The kinetic current density at 0.85 V of the Fe_2Mo/NC catalyst is as high as 82.28 mA/cm^2, which is 21-fold greater than that of the commercial Pt/C. It is interesting that the Fe_2Mo/NC catalyst, which possesses much less ORR active metal-N sites, exhibits 5.2-fold higher kinetic current density at 0.85 V than that of the Fe/NC catalyst, indicating that the Fe_2Mo bimetallic surface of Fe_2Mo/NC is energetically favorable for ORR (Fig.2(d) and Fig. S12 in the ESM) [45]. The durability of the Fe_2Mo/NC, Fe/NC and Pt/C catalysts are evaluated using accelerated durability test (ADT) by potential cycling between 0.6 and 1.0 V vs. RHE for 5,000 and 10,000 cycles in air-saturated 0.1 M KOH solution at a scan rate of 50 mV/s (Figs. 2(e) and 2(f), and Fig. S13 in the ESM). The Fe_2Mo/NC catalyst exhibits excellent durability in alkaline electrolyte, as evidenced by the loss of only 3 mV in $E_{1/2}$ after 10,000 potential cycles, which is much lower than that of Pt/C (29 mV loss in $E_{1/2}$).

In O_2 saturated 0.5 M H_2SO_4 solution, the Fe_2Mo/NC catalyst exhibits a more positive oxygen reduction peak (Fig. S14 in the ESM) and $E_{1/2}$ than that of Fe/NC (Fig. 3(a)). $E_{1/2}$ in the ORR polarization curve for Fe_2Mo/NC catalyst is 0.80 V, which is 6 and 12 mV higher than that of the commercial Pt/C and Fe/NC catalysts, respectively, indicating a comparable ORR electrocatalytic activity for the Fe_2Mo/NC catalyst with that of Pt/C. RRDE measurement and Koutecky–Levich plot demonstrate that the Fe_2Mo/NC catalyst exhibits a low H_2O_2 yield of 3.75% with the electron-transfer number of about 3.9, suggesting a four-electron ORR pathway (Fig. 3(b) and Fig. S15 in the ESM). As shown in Fig. 3(c), the Fe_2Mo/NC catalyst possesses a lower Tafel slope (57 mV/dec) than those of Fe/NC (70 mV/dec) and Pt/C (86 mV/dec) catalysts, indicating a favorable ORR electrocatalytic kinetics of the Fe_2Mo/NC catalyst in an acidic environment. The kinetic current density at 0.75 V for the Fe_2Mo/NC catalyst is 4-fold and 3.6-fold greater than those of the commercial Pt/C and Fe/NC catalysts, respectively, further supporting more energetically favorable ORR catalysis of Fe_2Mo/NC than those of Fe/NC and Pt/C (Fig. 3(d) and Fig. S16 in the ESM). The Fe_2Mo/NC catalyst also exhibits superior durability in the acidic electrolyte, as evidenced by the loss of 19 mV in $E_{1/2}$ after 10,000 potential cycles, which is lower than those of Fe/NC (21 mV loss in $E_{1/2}$) and Pt/C (26 mV loss in $E_{1/2}$) catalysts (Fig. 3(e), and Figs. S17 and S18 in the ESM). SEM-EDS analysis indicates the decrease of the Fe and Mo contents after the accelerated cycling test in acidic media (Table S2 in the ESM). The Fe_2Mo/NC catalyst exhibits the highest half-wave potentials in both acidic and alkaline electrolytes (0.8 V in 0.5 M H_2SO_4 and 0.91 V in 0.1 M KOH at 1,600 rpm, respectively) among the tested catalysts, which are even markedly higher than those of most newly reported highly active ORR catalysts, suggesting that the ORR electrocatalytic performance of Fe_2Mo/NC catalyst is among the best range for the non-PGM catalysts (Fig. 3(f) and Table S3 in the ESM).

Then we have introduced DFT to study the significant improvement of ORR performance by the formation of FeMo alloy. Within the (103) surface of the Fe_2Mo alloy, the surface electronic demonstrates an electron-rich feature, supporting a high electroactivity near the formed alloy particle. This is due to the existence of large amounts of step metal sites with unsaturated coordination, which supplies sufficient active sites to promote the ORR process (Fig. 4(a)). Then, we further look into the electronic structures of the metal alloy based on the projected partial density of states. Notably, both Fe-3d and Mo-4d orbitals locate near the Fermi level (E_F) with a high electron density, resulting in a good electron conductivity from the surface adsorbed intermediates to the electrode. Moreover, Fe-3d and Mo-4d orbitals achieve

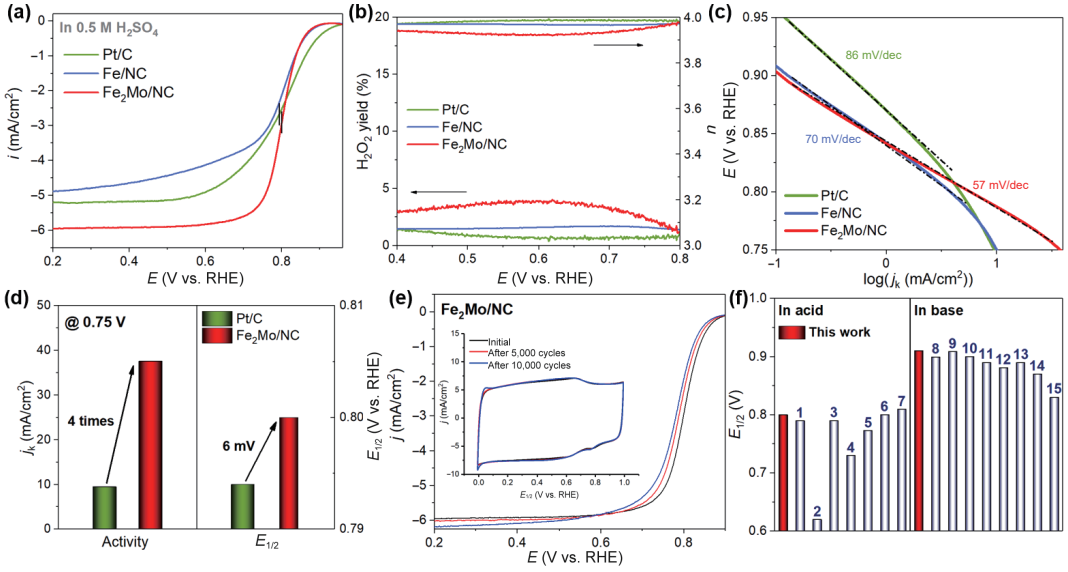

Figure 3 Performance of catalysts for the oxygen reduction in acidic media. (a) Linear voltammetry curves of commercial Pt/C, Fe/NC, and Fe_2Mo/NC catalysts recorded in O_2-saturated 0.5 M H_2SO_4 at 1,600 rpm. (b) Electron transfer number and peroxide yield calculated from the RRDE measurements for Pt/C, Fe/NC, and Fe_2Mo/NC catalysts. (c) Mass transport corrected Tafel plots of commercial Pt/C, Fe/NC, and Fe_2Mo/NC catalysts recorded in O_2-saturated 0.5 M H_2SO_4 at 1,600 rpm. (d) Comparison of the kinetic current density at 0.75 V and half-wave potential for commercial Pt/C and Fe_2Mo/NC catalysts. (e) ORR polarization curves and (inset) corresponding CV curves of the Fe_2Mo/NC catalyst before and after 5,000 and 10,000 cycles between 0.6 and 1.0 V. (f) Comparison of half-wave potential on reported robust non-PGM catalysts, including (1) for Fe-N-C (at 1,200 rpm) [46], (2) for Fe-N-C [30], (3) for Fe-N-C (at 900 rpm) [31], (4) for Co-N-C (at 900 rpm) [47], (5) for Co-NPs/HNCS [48], (6) for Mn-N-C [20], (7) for PANI-FeCo-C (at 900 rpm) [22] in 0.5 M H_2SO_4 electrolyte, (8) for Fe@C-FeNCs-2 [49], (9) Fe-SAs-N/C-*x* [28], (10) for FePc [12], (11) for FePc/$Ti_3C_2T_x$ [50], (12) for Co SAs/N-C(900) [51], (13) for CoFe alloy particles [36], (14) for NCNTFs [52], and (15) for PcCu-O_8-Co [53] in 0.1 M KOH/NaOH electrolyte.

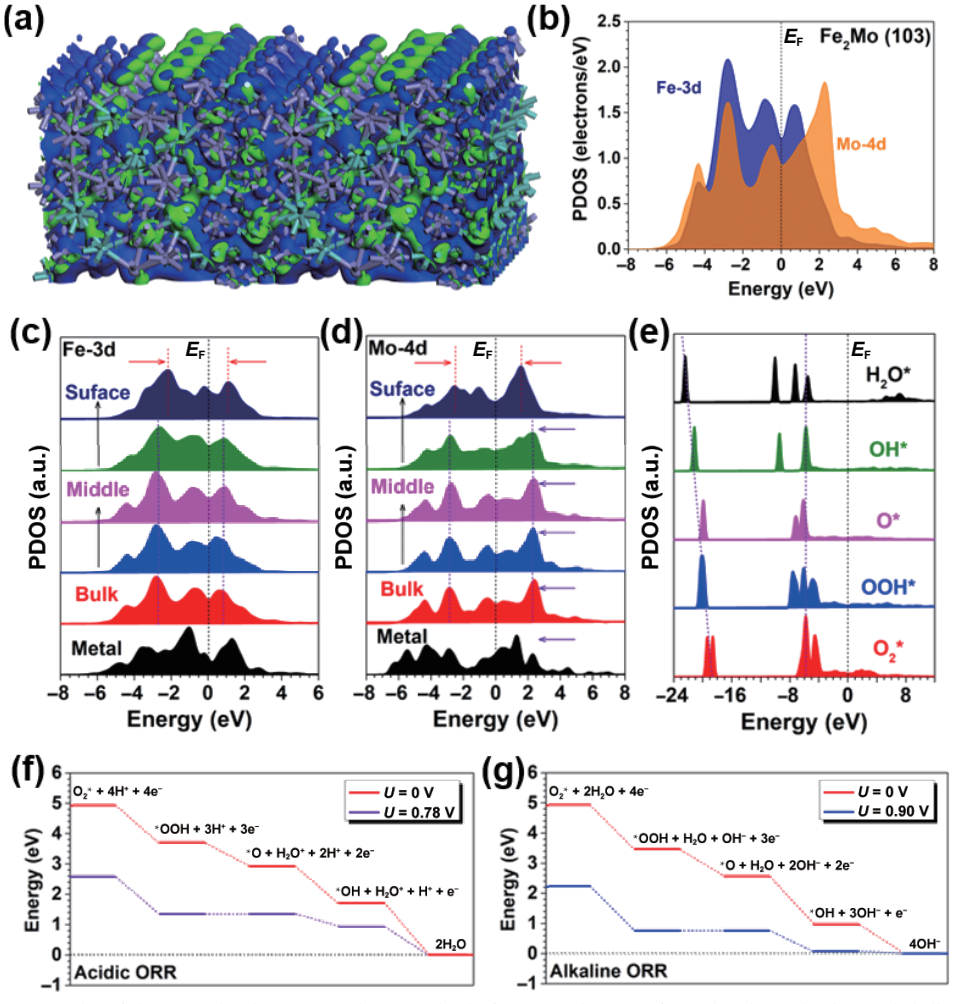

Figure 4 (a) The 3D contour plot of electronic distribution near the Fermi level of Fe2Mo. Blue isosurface = bonding orbitals. Purple ball = Fe, Cyan balls = Mo. Green isosurface = anti-bonding orbitals. (3D) contour plot of electronic distribution near the Fermi level of Fe_2Mo. (b) The projected density of states (PDOS) of Fe_2Mo. (c) The site-dependent PDOS of Fe in (103) surface of Fe_2Mo. (d) The site-dependent PDOS of Mo in (103) surface of Fe_2Mo. (e) The PDOS of key intermediates of ORR. (f) Energetic pathway of ORR in the acidic environment. (g) Energetic pathway of ORR in the alkaline environment.

substantial overlapping, indicating the d–d coupling enables the fast electron transfer. Such an electronic structure endows the electrocatalyst with superior stability due to mutual protection between Fe and Mo during the ORR condition. This also explained the remarkable stability of experiments in the alkaline environment (Fig. 4(b)). Then, we further look into the site-dependent electronic structures of both Fe and Mo sites. Compared to the pure Fe metal, the bulk to near-surface Fe-3d orbitals in Fe_2Mo alloy display enlarged e_g–t_{2g} splitting with lower d-band center position, which supports a stable electronic environment. Meanwhile, the surface Fe-3d orbitals demonstrate an improved electroactivity for ORR with reduced e_g–t_{2g} splitting and increased electron density near E_F (Fig. 4(c)). With the formation of the alloy, Mo-4d orbitals have been significantly modulated, which shows a broad occupation from E_V − 6.0 eV to E_V + 6.0 eV. It is also noted that Mo-4d orbitals also exhibit the electron-rich feature to support the reduction process towards O_2. More importantly, the broad Mo-4d orbitals well protect the Fe-3d orbitals during the reduction environment (Fig. 4(d)). Then, we further investigate the electronic structures of key intermediates during the ORR. For both alkaline and acidic ORR, the key intermediates are the same including O_2*, *OOH, O*, *OH, and H_2O*. Thus, the electron transfer efficiency between the transformation of intermediates significantly determines the ORR performance. For all the intermediates, we notice one evident linear correlation along the reaction coordinates, in which one correlates to the σ orbitals of s and p bands. The stronger linear correlation along the reaction coordinates supports a higher efficiency of electron transfer between each reaction step. Following the reaction coordinates, we notice the clear downshifting of the σ orbitals, supporting the successful reduction of the intermediates with more electron-rich structures. Meanwhile, we also notice the pinned dominant peaks of the p–π orbital, which usually reveal the electroactivity of the lattice instead of the intermediates (Fig. 4(e)). Therefore, the optimized electronic structure of FeMo alloy not only realizes the efficient electron transfer but also optimizes the stability of the electrocatalyst.

On the other side, we also investigate the energetic pathway of ORR in both acidic and alkaline environments. Under the short-cut circuit of the cell (U = 0 V), all the reactions are strongly exothermic. However, by applying the equilibrium potential of 1.23 V, we are able to estimate the overpotential by the largest barrier of 0.45 eV for the acidic environment, which correlates to the reaction from [*OOH + $3H^+$ + $3e^-$] to [O* + $2H^+$ + H_2O + $2e^-$]. This result indicates that 0.78 V should be the highest potential for all the reaction steps to be exothermic, which is close to the experimental results (Fig. 4(f)). For the alkaline environment, the rate-determining step is also noted at the transformation from *OOH to O*, which displays an overpotential of 0.33 eV. Then, the required potential to reach the spontaneous reaction trend for ORR will be 0.90 eV, which is highly similar to the experimental characterizations (Fig. 4(g)). Therefore, the energetic pathways reveal the superior performances of the electrocatalyst in both acidic and alkaline environments.

3 Conclusions

In summary, we described a promising Fe_2Mo catalyst having high activity and high durability for the ORR electrocatalysis derived from the ZIF-8 precursor. HRTEM and XPS analyses proved the distinct microstructure of Fe_2Mo/NC catalyst with Fe_2Mo nanoparticles as the core, nitrogen doped carbon as the shell. The as-prepared Fe_2Mo/NC catalyst possessed more effective hydrogenation of OH_{ad} on its Fe_2Mo surface than and commercial Pt/C single metallic Fe/NC catalysts with lower Tafel slopes and higher half-wave potentials in both alkaline and acidic environment. The Fe_2Mo/NC catalyst exhibits high kinetic current densities of 82.28 mA/cm^2 at 0.85 V in 0.1 M KOH solution and 37.62 mA/cm^2 at 0.75 V in 0.5 M H_2SO_4 solution, which are 21-fold and 4-fold greater than those of the commercial Pt/C, respectively. Furthermore, the Fe_2Mo/NC catalyst can largely retain the ORR activity after 10,000 potential cycles demonstrating its excellent long-term durability. DFT calculations have revealed that the formed Fe_2Mo alloy shows a high electroactivity towards the ORR process in both acidic and alkaline environments. The superior ORR originates from the d–d orbital coupling between Fe and Mo, which forms electroactive catalysts with strong stability for long-term application.

Acknowledgements

This research was supported by the National Key R&D Program of China (No. 2021YFA1501101), the National Nature Science Foundation of China (Nos. 21862011, 21771156, and 51864024) and Yunnan province (No. 2019FI003), the Shenzhen Knowledge Innovation Program (Basic Research, No. JCYJ20190808181205752), the Research Grants Council (RGC) of the Hong Kong Special Administrative Region, China (Project No. CityU 11206520), the National Natural Science Foundation of China/RGC Joint Research Scheme (No. N_PolyU502/21), and the funding for Projects of Strategic Importance of The Hong Kong Polytechnic University (Project Code: 1-ZE2V).

Electronic Supplementary Material: Supplementary material (Experimental section and calculation setup; XRD, HRTEM, and XPS results of comparison samples; electrochemical characterizations) is available in the online version of this article at https://doi.org/10.1007/s12274-022-4112-1.

References

[1] Gasteiger, H. A.; Marković, N. M. Just a dream—Or future reality? *Science* **2009**, *324*, 48–49.

[2] Debe, M. K. Electrocatalyst approaches and challenges for automotive fuel cells. *Nature* **2012**, *486*, 43–51.

[3] Hernandez-Fernandez, P.; Masini, F.; McCarthy, D. N.; Strebel, C. E.; Friebel, D.; Deiana, D.; Malacrida, P.; Nierhoff, A.; Bodin, A.; Wise, A. M. et al. Mass-selected nanoparticles of Pt_xY as model catalysts for oxygen electroreduction. *Nat. Chem.* **2014**, *6*, 732–738.

[4] Chen, C.; Kang, Y. J.; Huo, Z. Y.; Zhu, Z. W.; Huang, W. Y.; Xin, H. L.; Snyder, J. D.; Li, D. G.; Herron, J. A.; Mavrikakis, M. et al. Highly crystalline multimetallic nanoframes with three-dimensional electrocatalytic surfaces. *Science* **2014**, *343*, 1339–1343.

[5] Zhang, L.; Roling, L. T.; Wang, X.; Vara, M.; Chi, M.; Liu, J. Y.; Choi, S. I.; Park, J.; Herron, J. A.; Xie, Z. X. et al. Platinum-based nanocages with subnanometer-thick walls and well-defined, controllable facets. *Science* **2015**, *349*, 412–416.

[6] Huang, X. Q.; Zhao, Z. P.; Cao, L.; Chen, Y.; Zhu, E. B.; Lin, Z. Y.; Li, M. F.; Yan, A. M.; Zettl, A.; Wang, Y. M. et al. High-performance transition metal-doped Pt_3Ni octahedra for oxygen reduction reaction. *Science* **2015**, *348*, 1230–1234.

[7] Hu, J.; Wu, L. J.; Kuttiyiel, K. A.; Goodman, K. R.; Zhang, C. X.; Zhu, Y. M.; Vukmirovic, M. B.; White, M. G.; Sasaki, K.; Adzic, R. R. Increasing stability and activity of core–shell catalysts by preferential segregation of oxide on edges and vertexes: Oxygen reduction on Ti-Au@Pt/C. *J. Am. Chem. Soc.* **2016**, *138*, 9294–9300.

[8] Gong, K. P.; Du, F.; Xia, Z. H.; Durstock, M.; Dai, L. M. Nitrogen-doped carbon nanotube arrays with high electrocatalytic activity for oxygen reduction. *Science* **2009**, *323*, 760–764.

[9] Wang, Y.; Yang, Y.; Jia, S. F.; Wang, X. M.; Lyu, K. J.; Peng, Y. Q.; Zheng, H.; Wei, X.; Ren, H.; Xiao, L. et al. Synergistic Mn-Co catalyst outperforms Pt on high-rate oxygen reduction for alkaline polymer electrolyte fuel cells. *Nat. Commun.* **2019**, *10*, 1506.

[10] Deng, D. H.; Yu, L.; Chen, X. Q.; Wang, G. X.; Jin, L.; Pan, X. L.;

Deng, J.; Sun, G. Q.; Bao, X. H. Iron encapsulated within pod-like carbon nanotubes for oxygen reduction reaction. *Angew. Chem., Int. Ed.* **2013**, *52*, 371–375.
[11] Pegis, M. L.; Wise, C. F.; Martin, D. J.; Mayer, J. M. Oxygen reduction by homogeneous molecular catalysts and electrocatalysts. *Chem. Rev.* **2018**, *118*, 2340–2391.
[12] Chen, K. J.; Liu, K.; An, P. D.; Li, H. J.; Lin, Y. Y.; Hu, J. H.; Jia, C. K.; Fu, J. W.; Li, H. M.; Liu, H. et al. Iron phthalocyanine with coordination induced electronic localization to boost oxygen reduction reaction. *Nat. Commun.* **2020**, *11*, 4173.
[13] Takasu, Y.; Suzuki, M.; Yang, H. S.; Ohashi, T.; Sugimoto, W. Oxygen reduction characteristics of several valve metal oxide electrodes in $HClO_4$ solution. *Electrochim. Acta* **2010**, *55*, 8220–8229.
[14] Cui, Z. M.; Li, Y. T.; Fu, G. T.; Li, X.; Goodenough, J. B. Robust Fe_3Mo_3C supported IrMn clusters as highly efficient bifunctional air electrode for metal–air battery. *Adv. Mater.* **2017**, *29*, 1702385.
[15] Tan, H. B.; Li, Y. Q.; Kim, J.; Takei, T.; Wang, Z. L.; Xu, X. T.; Wang, J.; Bando, Y.; Kang, Y. M.; Tang, J. et al. Sub-50 nm iron-nitrogen-doped hollow carbon sphere-encapsulated iron carbide nanoparticles as efficient oxygen reduction catalysts. *Adv. Sci.* **2018**, *5*, 1800120.
[16] Guan, B. Y.; Yu, L.; Lou, X. W. A dual-metal–organic-framework derived electrocatalyst for oxygen reduction. *Energy Environ. Sci.* **2016**, *9*, 3092–3096.
[17] Amiinu, I. S.; Pu, Z. H.; Liu, X. B.; Owusu, K. A.; Monestel, H. G. R.; Boakye, F. O.; Zhang, H. N.; Mu, S. C. Multifunctional Mo-N/C@MoS_2 electrocatalysts for HER, OER, ORR, and Zn–air batteries. *Adv. Funct. Mater.* **2017**, *27*, 1702300.
[18] Kreider, M. E.; Stevens, M. B.; Liu, Y. Z.; Patel, A. M.; Statt, M. J.; Gibbons, B. M.; Gallo, A.; Ben-Naim, M.; Mehta, A.; Davis, R. C. et al. Relationships in molybdenum nitride electrocatalysts for the oxygen reduction reaction. *Chem. Mater.* **2020**, *32*, 2946–2960.
[19] Chen, Y. J.; Ji, S. F.; Zhao, S.; Chen, W. X.; Dong, J. C.; Cheong, W. C.; Shen, R. A.; Wen, X. D.; Zheng, L. R.; Rykov, A. I. et al. Enhanced oxygen reduction with single-atomic-site iron catalysts for a zinc–air battery and hydrogen–air fuel cell. *Nat. Commun.* **2018**, *9*, 5422.
[20] Li, J. Z.; Chen, M. J.; Cullen, D. A.; Hwang, S.; Wang, M. Y.; Li, B. Y.; Liu, K. X.; Karakalos, S.; Lucero, M.; Zhang, H. G. et al. Atomically dispersed manganese catalysts for oxygen reduction in proton-exchange membrane fuel cells. *Nat. Catal.* **2018**, *1*, 935–945.
[21] Xue, J. L.; Li, Y. S.; Hu, J. Nanoporous bimetallic Zn/Fe-N-C for efficient oxygen reduction in acidic and alkaline media. *J. Mater. Chem. A* **2020**, *8*, 7145–7157.
[22] Wu, G.; More, K. L.; Johnston, C. M.; Zelenay, P. High-performance electrocatalysts for oxygen reduction derived from polyaniline, iron, and cobalt. *Science* **2011**, *332*, 443–447.
[23] Yang, Z. K.; Wang, Y.; Zhu, M. Z.; Li, Z. J.; Chen, W. X.; Wei, W. C.; Yuan, T. W.; Qu, Y. T.; Xu, Q.; Zhao, C. M. et al. Boosting oxygen reduction catalysis with Fe-N_4 sites decorated porous carbons toward fuel cells. *ACS Catal.* **2019**, *9*, 2158–2163.
[24] Hu, Y. Z.; Lu, Y.; Zhao, X. R.; Shen, T.; Zhao, T. H.; Gong, M. X.; Chen, K.; Lai, C. L.; Zhang, J.; Xin, H. L. et al. Highly active N-doped carbon encapsulated Pd-Fe intermetallic nanoparticles for the oxygen reduction reaction. *Nano Res.* **2020**, *13*, 2365–2370.
[25] Li, J. Y.; Wang, G. X.; Wang, J.; Miao, S.; Wei, M. M.; Yang, F.; Yu, L.; Bao, X. H. Architecture of PtFe/C catalyst with high activity and durability for oxygen reduction reaction. *Nano Res.* **2014**, *7*, 1519–1527.
[26] Wang, Y.; Zheng, X. B.; Wang, D. S. Design concept for electrocatalysts. *Nano Res.* **2021**.
[27] Sun, M. R.; Chen, C. L.; Wu, M. H.; Zhou, D. N.; Sun, Z. Y.; Fan, J. L.; Chen, W. X.; Li, Y. J. Rational design of Fe-N-C electrocatalysts for oxygen reduction reaction: From nanoparticles to single atoms. *Nano Res.* **2021**.
[28] Jiang, R.; Li, L.; Sheng, T.; Hu, G. F.; Chen, Y. G.; Wang, L. Y. Edge-site engineering of atomically dispersed Fe-N_4 by selective C–N bond cleavage for enhanced oxygen reduction reaction activities. *J. Am. Chem. Soc.* **2018**, *140*, 11594–11598.
[29] Zhang, H. G.; Hwang, S.; Wang, M. Y.; Feng, Z. X.; Karakalos, S.; Luo, L. L.; Qiao, Z.; Xie, X. H.; Wang, C. M.; Su, D. et al. Single atomic iron catalysts for oxygen reduction in acidic media: Particle size control and thermal activation. *J. Am. Chem. Soc.* **2017**, *139*, 14143–14149.
[30] Ferrero, G. A.; Preuss, K.; Marinovic, A.; Jorge, A. B.; Mansor, N.; Brett, D. J. L.; Fuertes, A. B.; Sevilla, M.; Titirici, M. M. Fe-N-doped carbon capsules with outstanding electrochemical performance and stability for the oxygen reduction reaction in both acid and alkaline conditions. *ACS Nano* **2016**, *10*, 5922–5932.
[31] Li, Q.; Xu, P.; Gao, W.; Ma, S. G.; Zhang, G. Q.; Cao, R. G.; Cho, J.; Wang, H. L.; Wu, G. Graphene/graphene-tube nanocomposites templated from cage-containing metal–organic frameworks for oxygen reduction in Li–O_2 batteries. *Adv. Mater.* **2014**, *26*, 1378–1386.
[32] Han, A. L.; Wang, X. J.; Tang, K.; Zhang, Z. D.; Ye, C. L.; Kong, K. J.; Hu, H. B.; Zheng, L. R.; Jiang, P.; Zhao, C. X. et al. An adjacent atomic platinum site enables single-atom iron with high oxygen reduction reaction performance. *Angew. Chem., Int. Ed.* **2021**, *60*, 19262–19271.
[33] Wang, J.; Wu, H. H.; Gao, D. F.; Miao, S.; Wang, G. X.; Bao, X. H. High-density iron nanoparticles encapsulated within nitrogen-doped carbon nanoshell as efficient oxygen electrocatalyst for zinc-air battery. *Nano Energy* **2015**, *13*, 387–396.
[34] Varnell, J. A.; Tse, E. C. M.; Schulz, C. E.; Fister, T. T.; Haasch, R. T.; Timoshenko, J.; Frenkel, A. I.; Gewirth, A. A. Identification of carbon-encapsulated iron nanoparticles as active species in non-precious metal oxygen reduction catalysts. *Nat. Commun.* **2016**, *7*, 12582.
[35] Kim, S. J.; Mahmood, J.; Kim, C.; Han, G. F.; Kim, S. W.; Jung, S. M.; Zhu, G. M.; De Yoreo, J. J.; Kim, G.; Baek, J. B. Defect-free encapsulation of Fe^0 in 2D fused organic networks as a durable oxygen reduction electrocatalyst. *J. Am. Chem. Soc.* **2018**, *140*, 1737–1742.
[36] Xiong, Y.; Yang, Y.; DiSalvo, F. J.; Abruña, H. D. Metal–organic-framework-derived Co-Fe bimetallic oxygen reduction electrocatalysts for alkaline fuel cells. *J. Am. Chem. Soc.* **2019**, *141*, 10744–10750.
[37] Liu, Q. B.; Du, L.; Fu, G. T.; Cui, Z. M.; Li, Y. T.; Dang, D.; Gao, X.; Zheng, Q.; Goodenough, J. B. Structurally ordered Fe_3Pt nanoparticles on robust nitride support as a high performance catalyst for the oxygen reduction reaction. *Adv. Energy Mater.* **2019**, *9*, 1803040.
[38] Stamenkovic, V. R.; Fowler, B.; Mun, B. S.; Wang, G. F.; Ross, P. N.; Lucas, C. A.; Marković, N. M. Improved oxygen reduction activity on $Pt_3Ni(111)$ via increased surface site availability. *Science* **2007**, *315*, 493–497.
[39] Wang, X. X.; Cullen, D. A.; Pan, Y. T.; Hwang, S.; Wang, M. Y.; Feng, Z. X.; Wang, J. Y.; Engelhard, M. H.; Zhang, H. G.; He, Y. H. et al. Nitrogen-coordinated single cobalt atom catalysts for oxygen reduction in proton exchange membrane fuel cells. *Adv. Mater.* **2018**, *30*, 1706758.
[40] Hu, J.; Meng, Y. D.; Zhang, C. X.; Fang, S. D. Plasma-polymerized alkaline anion-exchange membrane: Synthesis and structure characterization. *Thin Solid Films* **2011**, *519*, 2155–2162.
[41] Jiao, L.; Wan, G.; Zhang, R.; Zhou, H.; Yu, S. H.; Jiang, H. L. From metal–organic frameworks to single-atom Fe implanted N-doped porous carbons: Efficient oxygen reduction in both alkaline and acidic media. *Angew. Chem., Int. Ed.* **2018**, *57*, 8525–8529.
[42] Huang, Y. C.; Ge, J. X.; Hu, J.; Zhang, J. W.; Hao, J.; Wei, Y. G. Nitrogen-doped porous molybdenum carbide and phosphide hybrids on a carbon matrix as highly effective electrocatalysts for the hydrogen evolution reaction. *Adv. Energy Mater.* **2018**, *8*, 1701601.
[43] Wang, B. W.; Wang, X. X.; Zou, J. X.; Yan, Y. C.; Xie, S. H.; Hu, G. Z.; Li, Y. G.; Dong, A. G. Simple-cubic carbon frameworks with atomically dispersed iron dopants toward high-efficiency oxygen reduction. *Nano Lett.* **2017**, *17*, 2003–2009.
[44] Yang, L.; Cheng, D. J.; Xu, H. X.; Zeng, X. F.; Wan, X.; Shui, J. L.; Xiang, Z. H.; Cao, D. P. Unveiling the high-activity origin of single-atom iron catalysts for oxygen reduction reaction. *Proc. Natl. Acad. Sci. USA* **2018**, *115*, 6626.

[45] Li, J. K.; Sougrati, M. T.; Zitolo, A.; Ablett, J. M.; Oğuz, I. C.; Mineva, T.; Matanovic, I.; Atanassov, P.; Huang, Y.; Zenyuk, I. et al. Identification of durable and non-durable FeN_x sites in Fe-N-C materials for proton exchange membrane fuel cells. *Nat. Catal.* **2021**, *4*, 10–19.

[46] Serov, A.; Artyushkova, K.; Atanassov, P. Fe-N-C oxygen reduction fuel cell catalyst derived from carbendazim: Synthesis, structure, and reactivity. *Adv. Energy Mater.* **2014**, *4*, 1301735.

[47] Fu, X. G.; Choi, J. Y.; Zamani, P.; Jiang, G. P.; Hoque, M. A.; Hassan, F. M.; Chen, Z. W. Co-N decorated hierarchically porous graphene aerogel for efficient oxygen reduction reaction in acid. *ACS Appl. Mater. Interfaces* **2016**, *8*, 6488–6495.

[48] Han, Y. H.; Wang, Y. G.; Chen, W. X.; Xu, R. R.; Zheng, L. R.; Zhang, J.; Luo, J.; Shen, R. A.; Zhu, Y. Q.; Cheong, W. C. et al. Hollow N-doped carbon spheres with isolated cobalt single atomic sites: Superior electrocatalysts for oxygen reduction. *J. Am. Chem. Soc.* **2017**, *139*, 17269–17272.

[49] Strickland, K.; Miner, E.; Jia, Q. Y.; Tylus, U.; Ramaswamy, N.; Liang, W. T.; Sougrati, M. T.; Jaouen, F.; Mukerjee, S. Highly active oxygen reduction non-platinum group metal electrocatalyst without direct metal–nitrogen coordination. *Nat. Commun.* **2015**, *6*, 7343.

[50] Li, Z. L.; Zhuang, Z. C.; Lv, F.; Zhu, H.; Zhou, L.; Luo, M. C.; Zhu, J. X.; Lang, Z. Q.; Feng, S. H.; Chen, W. et al. The marriage of the FeN_4 moiety and mxene boosts oxygen reduction catalysis: Fe 3d electron delocalization matters. *Adv. Mater.* **2018**, *30*, 1803220.

[51] Yin, P. Q.; Yao, T.; Wu, Y. E.; Zheng, L. R.; Lin, Y.; Liu, W.; Ju, H. X.; Zhu, J. F.; Hong, X.; Deng, Z. X. et al. Single cobalt atoms with precise N-coordination as superior oxygen reduction reaction catalysts. *Angew. Chem., Int. Ed.* **2016**, *128*, 10958–10963.

[52] Xia, B. Y.; Yan, Y.; Li, N.; Wu, H. B.; Lou, X. W.; Wang, X. A metal–organic framework-derived bifunctional oxygen electrocatalyst. *Nat. Energy* **2016**, *1*, 15006.

[53] Zhong, H. X.; Ly, K. H.; Wang, M. C.; Krupskaya, Y.; Han, X. C.; Zhang, J. C.; Zhang, J.; Kataev, V.; Büchner, B.; Weidinger, I. M. et al. A phthalocyanine-based layered two-dimensional conjugated metal–organic framework as a highly efficient electrocatalyst for the oxygen reduction reaction. *Angew. Chem., Int. Ed.* **2019**, *131*, 10787–10792.